

# MASKSEARCH: Querying Image Masks at Scale

Dong He, Jieyu Zhang, Maureen Daum, Alexander Ratner, Magdalena Balazinska  
University of Washington, {donghe, jieyuz2, mdaum, ajratner, magda}@cs.washington.edu

## ABSTRACT

Machine learning tasks over image databases often generate masks that annotate image content (e.g., saliency maps, segmentation maps) and enable a variety of applications (e.g., determine if a model is learning spurious correlations or if an image was maliciously modified to mislead a model). While queries that retrieve examples based on mask properties are valuable to practitioners, existing systems do not support such queries efficiently. In this paper, we formalize the problem and propose a system, MASKSEARCH, that focuses on accelerating queries over databases of image masks. MASKSEARCH leverages a novel indexing technique and an efficient filter-verification query execution framework. Experiments on real-world datasets with our prototype show that MASKSEARCH, using indexes approximately 5% the size of the data, accelerates individual queries by up to two orders of magnitude and consistently outperforms existing methods on various multi-query workloads that simulate dataset exploration and analysis processes.

## 1 INTRODUCTION

Many machine learning (ML) tasks over image databases commonly generate masks that annotate individual pixels in images. For instance, model explanation techniques [53–56, 65] generate saliency maps or feature importance maps to highlight the significance of individual pixels to a model’s output (e.g., pixels that correspond to the head of an animal might most contribute to the classification of that animal as a given species). In image segmentation tasks [27, 36, 49], masks denote the probability of pixels being associated with a specific class or instance. Depth estimation models [9, 44] yield masks reflecting the depth of each pixel, while human pose estimation models [14, 22] provide masks indicating the probability of pixels corresponding to body joints. These are just a few examples of how masks play a crucial role in diverse ML tasks, among many others.

Studying the properties of these masks can unlock a wide range of applications across various domains. For example, in the context of model explanation, examining saliency maps is the most common approach to understand whether the model is relying on spurious correlations in the input data [46], which are signals in the input data that do not align well with domain knowledge [11, 18, 42, 43, 60]. In [18], the authors studied saliency maps generated for chest X-ray images and found that models trained to detect COVID-19 based on the chest radiographs were relying on confounding factors, i.e., markers in the background of the X-rays, rather than the medical pathology, to make their predictions. They observed that the high-value pixels in the saliency maps were concentrated around the edges of the X-ray images, which indicates that the model was relying on spurious correlations instead of the lung regions to make its prediction, leading to poor generalizability to X-rays from new hospitals. Other applications based on the properties of masks include identifying maliciously attacked examples using saliency maps [59, 63, 64],

out-of-distribution detection using saliency maps [30], monitoring model errors in production [1, 3, 35], traffic monitoring and retail analytics using segmentation masks [2, 4], and many more.

Considering the importance of mask properties in these applications, queries that retrieve examples from the dataset based on such properties are valuable to ML researchers and practitioners [17, 36, 46]. These queries facilitate the aforementioned applications by enabling users to identify examples that satisfy certain mask properties interactively. For example, Meta’s Segment Anything [36] allows users to query for images and segmentation masks based on the mask area and the number of masks per image. In the chest X-ray example, a doctor may want to identify examples for which the model is not relying on the lung regions to make its prediction. They could then ask, which chest X-ray images have saliency maps with more high-value pixels outside the lung region than inside that region? The returned examples can then be used to investigate the spurious correlations that the model relies on and improve the model’s generalizability.

Unfortunately, despite numerous applications that arise from querying examples based on mask properties, there is a lack of system support for these queries [29]. For example, according to [46], to identify examples for which the model relies on spurious correlations, researchers have to manually examine the explanation maps for each image, which is a tedious process.

Efficiently executing these queries is challenging. The fundamental operations in these queries involve filtering masks based on the number of pixels within regions of interest (ROI) and pixel value ranges. For example, in the case of chest X-rays, a user might want to find all masks with a large number of salient pixels outside the lung region. The key challenge is that the database of masks is too large to fit in memory, and loading all masks from disk and processing them is slow and dominates the query execution time. Existing methods and systems do not support these queries efficiently. For instance, using NumPy to load and process the masks, a query that filters masks based on the number of pixels within an ROI and a pixel value range takes more than 30 minutes to complete on the ImageNet dataset (see Figure 5), and we find that loading compressed masks does not solve the problem due to the time required for decompressing the masks before processing.

While existing relational database systems, e.g., PostgreSQL, can support these queries through user-defined functions, they also exhibit slow execution times, taking over 30 minutes for a single query on the ImageNet dataset (see Figure 5). Existing multi-dimensional indexing techniques also do not provide better execution times because masks are dense arrays. Additionally, these techniques are unable to support mask-specific ROIs, i.e., different ROIs for different masks, in a single query, which is a common scenario in many applications, e.g., image classification model developers may want to find examples for which the model is not relying on the foreground objects to make its prediction. In this case, the ROI is the foreground object, which differs for different masks.

Although array database systems such as SciDB [13] are designed to process multi-dimensional dense arrays, they are not optimized for efficiently searching through large collections of arrays, as required in these queries. The techniques proposed in this paper can be integrated into existing systems to enhance their performance.

In this paper, we propose MASKSEARCH, a system that accelerates the aforementioned queries. MASKSEARCH introduces a new type of index and an efficient filter-verification query execution framework. Both techniques work in tandem to reduce the number of masks that are loaded from disk during query execution. The indexing technique, which we call the Cumulative Histogram Index (CHI), provides bounds on the pixel counts within an ROI and a pixel value range in a mask. It is designed to work for arbitrary ROIs and pixel value ranges specified by the user at query time. These bounds are useful when deciding whether a mask should be loaded from disk during query execution.

MASKSEARCH’s query execution employs the idea of pre-filtering. Using pre-filtering techniques to avoid expensive computation or disk I/O has been explored and proved to be effective in many other problems, such as accelerating similarity joins [32, 39] and queries that contain ML models [6, 31, 34, 38] in cases where computing the similarity function or running the model is expensive during query execution. MASKSEARCH’s filter-verification query execution framework leverages the CHI to bypass loading the masks that are guaranteed to satisfy or not satisfy the query predicate. Only the masks that cannot be filtered out are loaded from disk, and the query predicate is applied to them. By doing so, MASKSEARCH overcomes the limitations of existing systems by significantly reducing the number of masks that are loaded from disk during query execution. Moreover, MASKSEARCH includes an incremental indexing approach that avoids potentially high upfront indexing costs and enables it to operate in an online setting.

Furthermore, we extend MASKSEARCH’s capabilities to support aggregations and top- $k$  computations and accordingly optimize the query execution for them. Aggregations are often used to compare the trends of different masks, e.g., studying the difference between model saliency maps and human attention maps for visual question answering [17]. Top- $k$  computations are also widely used because manual inspection of large volumes of query results is increasingly untenable [5]. Example queries include finding the top- $k$  X-rays whose saliency maps have the least number of high-value pixels in the lung regions.

In summary, the contributions of this paper are:

- We formalize a novel, and broadly applicable, class of queries that retrieve images from a dataset based on the properties of masks computed over those images, and further extend the queries to support aggregations and top- $k$  computations (§2).
- We design and implement MASKSEARCH, a system that accelerates these queries by leveraging a novel indexing technique and an efficient filter-verification query execution framework (§3).
- We evaluate MASKSEARCH with extensive experiments on real-world datasets. We demonstrate that MASKSEARCH achieves up to two orders of magnitude speedup over existing methods for individual queries, and consistently outperforms existing

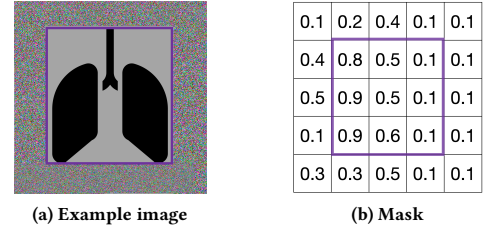


**Figure 1: A toy image motivated by [18] and its mask. The purple box is the ROI. Predicates on masks often involve counting the number of pixels in the ROI with values in a range, e.g., # pixels in the ROI with values in  $(0.85, 1.0)$  is 2.**

methods on various multi-query workloads that simulate dataset exploration and analysis processes (§4).

Overall, MASKSEARCH is an important next step toward the seamless and rapid exploration of a dataset based on masks generated by ML models. It is an important component in a toolbox of methods for ML model explainability and debugging.

## 2 QUERIES OVER MASKS

In this section, we start by presenting example scenarios that require queries over image masks, motivated by applications from the literature. We then formalize this class of queries and discuss the challenges associated with their efficient execution.

### 2.1 Example Applications

**Example 1: Identifying images with spurious correlations.** Consider image classification applications, such as the example of X-ray images from [18] that we introduced above, where the classifier needs to distinguish COVID from Non-COVID, and other traditional image classifiers [28]. In those applications, it is important to ensure that models are learning proper object features and are not relying on spurious correlations at the periphery [11, 43, 60], such as annotations indicating the sources of the images [18] or background, such as water or snow [42, 48]. Saliency maps can serve to determine the importance of different pixels to the model output and perform such verifications. Figure 1 shows a toy version of such an image with its mask, illustrating an object and potential background noise. To ensure that a model is classifying the image based on the properties of the object, a developer can look at the number of mask pixels with high values within the bounding box of the object and compare that number to either the area of the object or the total number of mask pixels with high values. A developer could further query for the top- $k$  images where such ratios are highest or lowest. Concretely, a query over our toy example could count the number of pixels with values higher than 0.85 in the bounding box, which produces a count of two pixels, and compare against the area, which is 6 pixels, for a ratio of 0.33. The query could return all images with a ratio below some threshold or could return the images with the lowest ratios.

**Example 2: Comparing model saliency maps and human attention maps.** Motivated by [17], to understand whether visual question answering (VQA) models and humans focus on the same parts of an image to answer a question, a researcher may want to

compare the saliency maps of a VQA model and human attention maps. To achieve this, they can generate saliency maps for the VQA model and human attention maps for the same images, and then issue a query to retrieve images with the highest number of pixels with values above some threshold in the intersection of the two masks. The returned images are those for which the VQA model and humans focus on the same parts of the image to answer a question.

## 2.2 Query Formulation

MASKSEARCH is designed to support queries such as the aforementioned examples with predicates on image masks that apply filters and aggregations (i.e., count of pixels) on the values of pixels within regions of interest. It also supports aggregations over the pixel counts and pixel counts over aggregated masks.

We formalize this class of queries by capturing the data using the following simple relational view:

```
MasksDatabaseView (
  mask_id INTEGER PRIMARY KEY,
  image_id INTEGER,
  model_id INTEGER,
  mask_type INTEGER,
  mask REAL[][] ,
  ... );
```

With some abuse of notation, an example tuple in the above view could be (11, 77, ResNet50, SaliencyMap, [[0.9, 0.5, ...], ...]), referring to a saliency map computed for image #77 using ResNet50.

In this conceptual view, `mask_id`, `image_id`, and `model_id` store the unique identifiers of the mask, image, and model that generate the mask, respectively. `mask_type` is the identifier of the type of mask, e.g., saliency map, human attention map, segmentation mask, depth mask, etc. The `mask` column stores the mask itself. Each mask is a 2D array of floating points in the range of [0, 1). Additional columns can store other information, such as ground-truth labels, predicted labels, and image capture times.

The generic query can then be formulated as follows,

```
SELECT *, CP(mask, roi, (lv, uv)) as val
FROM MasksDatabaseView
WHERE <filter on CP(...)> [AND | OR] ... -- opt.
ORDER BY val [ASC | DESC] -- opt.
LIMIT K; -- opt.
```

**Region of interest (ROI).** The ROI, `roi`, is a bounding box represented by pairs of coordinates that are the upper left and lower right corners of the box. It can be constant for all masks or different for each mask (mask-dependent ROIs), e.g., the bounding box of the foreground object in each image. In practice, ROI is specified by the user at query time or obtained from another table joined with `MasksDatabaseView`. Moreover, the user can specify an arbitrary number of ROIs in a query.

**CP function.** At the core of the query is the CP function. It takes in a mask, an ROI, a lower bound (`lv`), and an upper bound (`uv`) as input, and returns the number of pixels in the ROI of the mask with values in the range of [`lv`, `uv`). CP is formally defined as follows,

$$CP(mask, roi, (lv, uv)) = \sum_{(x,y) \in roi} \mathbb{1}_{lv \leq mask[x][y] < uv}$$

where  $\mathbb{1}_{condition}$  is an indicator function that is 1 if the condition is true and 0 otherwise. Note that the output of CP is a scalar

value and arithmetic operations can be applied to it. In our target queries, CP is often present in the filter predicate, e.g.,  $CP(mask, roi, (lv, uv)) > T$ , and in the ORDER BY clause, e.g., ORDER BY  $CP(mask, roi, (lv, uv))$  ASC.

**Query in Example 1:** after setting `roi` to the bounding box of the foreground object for every mask, the query can be written as,

```
SELECT image_id, CP(mask, roi, (0.85, 1.0)) / area(roi) AS r
FROM MasksDatabaseView
ORDER BY r ASC LIMIT 25;
```

Motivated by Example 2 in §2.1, we further extend the query language to support aggregations,

```
SELECT [mask_id | image_id | model_id | ...],
  [SCALAR_AGG(CP(mask, roi, (lv, uv)))
  | CP(MASK_AGG(mask), roi, (lv, uv))] as aggregate
FROM MasksDatabaseView
WHERE <filter on CP(...)> [AND | OR] ... -- opt.
GROUP BY [image_id | model_id] -- opt.
HAVING <filter on aggregate> [AND | OR] ... -- opt.
ORDER BY aggregate [ASC | DESC] -- opt.
LIMIT K; -- opt.
```

**Aggregation functions.** The user can aggregate the outputs of CP functions for masks of different types (e.g., human attention maps and model saliency maps), and masks generated by different models by defining the `SCALAR_AGG` function, or aggregate the mask pixels directly by defining the `MASK_AGG` function.

**Scalar aggregation.** `SCALAR_AGG` is used to aggregate the outputs of CP functions. MASKSEARCH supports common functions such as SUM, AVG, MIN, and MAX.

**Mask aggregation.** `MASK_AGG` is used to aggregate masks themselves. It is a user-defined function that takes in a list of masks as input and returns a mask,

```
MASK_AGG(m_1: REAL[][] , ..., m_n: REAL[][] ) -> REAL[][]
```

Examples include  $INTERSECT(m_1 > 0.8, ..., m_n > 0.8)$ , i.e., the intersection of the masks after thresholding at 0.8.

**Query in Example 2:** we associate model saliency maps with `mask_type = 1` and human attention maps with `mask_type = 2`. After setting `roi` to the full mask, the query can be written as,

```
SELECT image_id, CP(INTERSECT(mask>0.7), roi, (0.7, 1.0)) AS s
FROM MasksDatabaseView WHERE mask_type IN (1, 2)
GROUP BY image_id
ORDER BY s DESC LIMIT 10;
```

## 2.3 Challenges

Processing the above queries efficiently is challenging. A baseline approach of loading masks from disk into memory before query processing is extremely slow because it saturates disk read bandwidth. For example, a single query on the ImageNet dataset takes more than 30 minutes to complete (see Figure 5). Alternatively, storing compressed masks on disk reduces data loaded from disk but moves the bottleneck to decompression, so executing a single query on ImageNet still takes around 30 minutes.

Existing systems, such as PostgreSQL, have the same bottleneck of loading masks from disk. Existing multi-dimensional indexing techniques do not efficiently support our target queries because the masks are dense arrays. They require treating each mask’s pixel as a point in the multi-dimensional space of ( $x$ ,  $y$ , pixel value), where  $x$  and  $y$  are the pixel’s coordinates. In such a space, our

query is essentially an orthogonal range query followed by an aggregate grouping by `mask_id`. The best existing algorithm [15, 16], range trees, has a query time complexity of  $O(k + \log^2 n)$  and a preprocessing time of  $O(n \log^2 n)$ , where  $n$  is the total number of mask pixels in the dataset, and  $k$  is the number of pixels in the cuboid defined by `roi` and  $(lv, uv)$ .  $n$  is large because our data is dense. For example, the total number of pixels in one set of masks for the ImageNet dataset (1 mask per image) is more than 65 billion, which makes using these indexes infeasible. Array databases, such as SciDB [13], are designed to work with dense arrays, but they are optimized for complex computations over small numbers of large arrays rather than efficiently searching through large numbers of arrays. While SciDB can load specific slices within a desired ROI rather than entire arrays, our system avoids loading any pixels at all for a large fraction of masks, as we explain next. We discuss related work further in §5.

### 3 MASKSEARCH

MASKSEARCH efficiently executes queries over a database of image masks. As presented above, the fundamental operations in our target queries involve filtering masks based on pixel values within regions of interest, followed by performing optional aggregations, sorting, or top- $k$  computations. The key challenge when performing these operations is that the database of masks is too large to fit in memory, and scanning, loading, and processing all masks is slow.

To accelerate such queries, MASKSEARCH introduces a novel type of index, called the Cumulative Histogram Index (CHI) (§3.1), and an efficient filter-verification query execution framework (§3.2).

The CHI technique indexes each mask by maintaining pixel counts for key combinations of spatial regions and pixel values. CHI constructs a compact data structure that provides fast computation of upper and lower bounds on CP functions for arbitrary regions of interest and pixel value ranges. These bounds are used in the query execution framework to efficiently filter out masks that are either guaranteed to fail the query predicate or guaranteed to satisfy it.

During the filter stage, the framework utilizes CHI to compute bounds on CP functions to filter out the masks without loading them from disk. Then, during the verification stage, the framework verifies the remaining masks by loading them from disk and applying the full predicate. This framework overcomes the bottleneck of query execution because it significantly reduces the number of masks loaded from disk during query execution.

#### 3.1 Cumulative Histogram Index (CHI)

The Cumulative Histogram Index (CHI) is designed to efficiently evaluate predicates over image masks without loading them, so as to minimize the number of masks that must be loaded from disk during query execution. Predicates over image masks have several components: (1) They consider the pixels within a given region of interest, which may depend on each specific mask, e.g., the output of an object detector on the corresponding image; (2) They focus on pixel values within a range, e.g., pixel values that correspond to an object detector confidence of at least 0.6; (3) They typically count the number of pixels that satisfy (1) and (2) and apply a final predicate on that count. As defined in §2, those predicates can be formally expressed as  $CP(mask, roi, (lv, uv)) > T$ .

The key goals of CHI are to: (G1) support arbitrary query parameters  $lv$  and  $uv$  that specify the range of pixel values, which are unknown to MASKSEARCH ahead of time, and (G2) support arbitrary regions of interest, `roi`, and allow mask-specific `rois` in a single query. The `rois` are also unknown ahead of time because the user can specify `rois` arbitrarily at query time.

**Key idea:** MASKSEARCH achieves both goals by building CHI to maintain pixel counts for different combinations of spatial locations and pixel values. Conceptually, MASKSEARCH builds an index on the search key  $(mask\_id, roi, \text{pixel value})$ . For each search key, the CHI holds the count of pixels that satisfy the condition. Given  $mask\_id$ , `roi`, and a range of pixel values specified by  $(lv, uv)$ , the index supports queries that return the number of pixels in the `roi` of the mask with values in the range  $(lv, uv)$ , i.e.,  $CP(mask, roi, (lv, uv))$ .

Building an index on every possible combination of  $(mask\_id, roi, \text{pixel value})$  is infeasible both in terms of space and time complexity because the number of possible `rois` for each mask is quadratic in the number of pixels in the mask, let alone the number of masks and the number of pixel values.

Instead, CHI builds a data structure that efficiently provides upper and lower bounds on predicates, rather than exact values. This approach leads to a small-size index while still effectively pruning masks that are either guaranteed to fail the predicate or guaranteed to satisfy it. Only a small fraction of masks must then be loaded from disk and processed in full to verify the predicate.

**CHI details:** CHI leverages two key ideas: discretization and cumulative counts. Discretization reduces the total amount of information in the index, while cumulative counts yield highly efficient lookups. We explain both here.

To build a small-sized index, MASKSEARCH partitions masks into disjoint regions and discretizes pixel values into disjoint intervals. It then builds an index on the combinations of  $(mask\_id, \text{region}, \text{pixel value interval})$ . For the spatial dimensions, MASKSEARCH partitions each mask into a grid of cells, each  $w_c$  by  $h_c$  pixels in size. For the pixel value dimension, MASKSEARCH discretizes the values into  $b$  buckets (bins). MASKSEARCH could use either equi-width or equi-depth buckets. Our current prototype uses equi-width buckets.

After discretization, there are several options for implementing the index. A straightforward option is to build an index on the search key  $(mask\_id, cx\_id, cy\_id, bin\_id)$ , where  $cx\_id$ ,  $cy\_id$ , and  $bin\_id$  identify the coordinates of each unique combination of grid and pixel-value range (e.g.,  $cx\_id$  of 3 corresponds to the grid cell that starts at pixel  $w_c * 3$ , similarly for  $cy\_id$  and  $bin\_id$ ). For each such key, the index could store the number of pixels in the mask whose coordinates are in the cell identified by  $(cx\_id, cy\_id)$  and with values in the range  $[p_{min} + bin\_id \cdot \Delta, p_{min} + (bin\_id + 1) \cdot \Delta)$ , where  $p_{min}$  is the lowest pixel value across all masks and  $\Delta$  is the width of each bucket. This option would require MASKSEARCH to identify all the cells that intersect with `roi` and all the bins that intersect with  $(lv, uv)$  and perform our query execution technique (discussed in §3.2) on the pixel counts of these cells and bins. A more efficient approach, which we adopt, is to build an index on the search key  $(mask\_id, cx\_id, cy\_id, bin\_id)$ , but, for each key, store the reverse cumulative sum of pixel counts in the mask with values in the range  $[p_{min} + bin\_id \cdot \Delta, p_{max}]$  and coordinates in the region of  $((1, 1), (cx\_id \cdot w_c, cy\_id \cdot h_c))$ . This



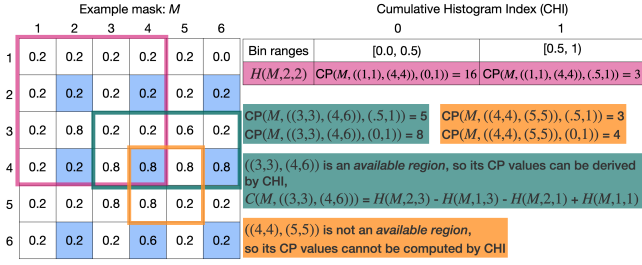


Figure 2: An example of CHI, CP, available region, and  $C$ .

index is denoted with  $H(mask\_id, cx\_id, cy\_id, bin\_id)$ . We will also use  $H(mask\_id, cx\_id, cy\_id)$  to denote the array of cumulative sums for all bins, i.e.,  $H(mask\_id, cx\_id, cy\_id)[bin\_id] = H(mask\_id, cx\_id, cy\_id, bin\_id)$ . Recall that  $mask\_id$  uniquely identifies  $mask$ . The index can be formally expressed as,

$$H(mask\_id, cx\_id, cy\_id, bin\_id) = CP(mask, ((1, 1), (cx\_id \cdot w_c, cy\_id \cdot h_c)), (p_{min} + bin\_id \cdot \Delta, p_{max})) \quad (1)$$

**Example:** In Figure 2, MASKSEARCH builds the CHI for an example mask,  $M$ , with  $w_c = 2$ ,  $h_c = 2$ , and  $b = 2$ . Hence, each cell,  $(x_c, y_c)$ , highlighted in light blue marks the corner of a discretized region. With  $b = 2$ , the pixel value range is discretized into  $b$  bins,  $[0, 0.5)$  and  $[0.5, 1)$ . MASKSEARCH builds  $H(M, x_c/w_c, y_c/h_c)$  for each of the corner cells. For example, for cell  $(2, 2)$ , we have  $H(M, 1, 1)[0] = 4$  (all four pixels are in  $(p_{min}, p_{max})$ ) and  $H(M, 1, 1)[1] = 0$  (no pixels are in the  $0.5$  to  $p_{max}$  range). For cell  $(4, 4)$ ,  $H(M, 2, 2) = [16, 3]$ .

In essence,  $H(mask\_id, cx\_id, cy\_id, bin\_id)$  stores a cumulative sum of pixel counts, considering both spatial and pixel value dimensions. Storing cumulative sums offers greater efficiency compared to storing raw values, as it enables rapid evaluation of pixel counts within a specific range, in terms of both spatial and pixel value dimensions, by only performing simple arithmetic operations. To illustrate this, we first introduce the concept of available regions.

**Definition 3.1.** Let  $X_c$  denote  $\{x_c | x_c \in [w_c, 2w_c, \dots, w]\}$  and  $Y_c$  denote  $\{y_c | y_c \in [h_c, 2h_c, \dots, h]\}$ . A region  $((x_1, y_1), (x_2, y_2))$  is available in the CHI of a mask if  $(x_2, y_2) \in X_c \times Y_c$  and  $(x_1 - 1, y_1 - 1) \in (X_c \cup \{0\}) \times (Y_c \cup \{0\})$ .

To compute pixel counts within an available region in the CHI with pixel values within the range of two bin boundaries, MASKSEARCH performs the following steps: (1) compute the reverse cumulative sums for the specified region using the index values; (2) calculate pixel counts between the two bin boundaries by subtracting the relevant cumulative sums.

We now describe the details of these steps. Let  $C(mask\_id, r)$  denote the histogram of the reverse cumulative pixel counts of region  $r$  in mask  $mask\_id$ , where  $C(mask\_id, r)[i] = CP(mask, r, (p_{min} + i\Delta, p_{max}))$ . MASKSEARCH can compute  $C(mask\_id, ((x_1, y_1), (x_2, y_2)))$  for any available region  $((x_1, y_1), (x_2, y_2))$ . Let  $m$  denote  $mask\_id$  for brevity, we have,

$$C(m, ((x_1, y_1), (x_2, y_2))) = H(m, x_2/w_c, y_2/h_c) - H(m, (x_1 - 1)/w_c, y_2/h_c) - H(m, x_2/w_c, (y_1 - 1)/h_c) + H(m, (x_1 - 1)/w_c, (y_1 - 1)/h_c) \quad (2)$$

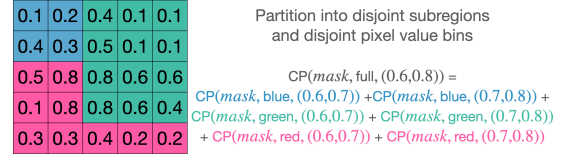


Figure 3: Illustration of CP being a (finitely)-additive function.

where  $-$  and  $+$  are element-wise subtraction and addition, respectively, for two arrays of the same size. Equation (2) holds because  $C(mask\_id, region)$  is a (finitely)-additive function over disjoint spatial partitions since each bin of  $C(mask\_id, region)$  is a CP function which is (finitely)-additive. Figure 3 shows an illustrative example of this additive property. Note that for any  $mask\_id$  and  $roi$ ,  $C(mask\_id, roi)[p_{max}/\Delta]$  is always 0 for notation simplicity.

**Example:** In Figure 2, an example available region is  $((3, 3), (4, 6))$ , highlighted with a dark green bounding box. An example non-available region is  $((4, 4), (5, 5))$ , highlighted with an orange bounding box.

After MASKSEARCH computes the reverse cumulative sums for a region  $r$ , the pixel counts between any two bin boundaries (for pixel value discretization) can be obtained by subtracting the cumulative sums of the two bins.

These steps are much faster than the computation required if the pixel counts were stored directly instead of the cumulative sums because it avoids the need to access all bins within the desired pixel value range for each cell in region  $r$ .

Given a predicate  $CP(mask, roi, (lv, uv)) > T$ , MASKSEARCH uses the CHI to check whether the predicate is satisfied. At a high level, MASKSEARCH identifies available regions,  $r_1$  and  $r_2$ , in the CHI of the mask, such that  $r_1$  is the smallest region that covers  $roi$  and  $r_2$  is the largest region that is covered by  $roi$ . Then, MASKSEARCH computes  $C(mask, r_1)$  and  $C(mask, r_2)$  using Equation (2) and uses them to compute the lower and upper bounds of  $CP(mask, roi, (lv, uv))$ . Finally, MASKSEARCH checks whether  $mask$  is guaranteed to satisfy or guaranteed to fail the predicate by comparing the lower and upper bounds with  $T$ . The details are further explained in §3.2.

Since  $mask\_id$ ,  $cx\_id$ ,  $cy\_id$ , and  $bin\_id$  are all integers, rather than building a B-tree index or a hash index over the keys, we create an optimized index structure using an array where  $mask\_id$ ,  $cx\_id$ ,  $cy\_id$ , and  $bin\_id$  act as offsets for lookups in the array. We call this structure the Cumulative Histogram Index (CHI) and  $H(mask\_id)$  the CHI of the mask  $mask\_id$ . There are several advantages of this optimized index structure. First, it enables MASKSEARCH to only store the values of CHI and avoid the cost of storing the keys of CHI and the overhead of building a B-tree or hash index. Second, for any lookup key, the lookup latency is of constant complexity and avoids pointer chasing which is common in other index structures.

The time complexity for computing the CHI for  $N$  masks of size  $w \times h$  is  $O(N \cdot w \cdot h)$ . The number of CHI that MASKSEARCH builds for  $N$  masks is  $N \cdot w \cdot h / (w_c \cdot h_c)$ . Each CHI has  $b$  bins, thus taking  $4 \cdot b$  bytes. Hence, the set of CHI of  $N$  masks takes  $4 \cdot b \cdot N \cdot w \cdot h / (w_c \cdot h_c)$  bytes in space. With a reasonable configuration of  $b$ ,  $w_c$ , and  $h_c$ , CHI can be held in memory for a moderately-sized dataset, and MASKSEARCH can achieve good query performance with it. For example, it only takes approximately 6.5 GB of memory to hold

the CHI of ImageNet (1 mask per image, 1.3 M masks in total) with  $b = 16$ ,  $w_c = 28$ , and  $h_c = 28$ . As shown in §4.2, with such a configuration, MASKSEARCH achieves two orders of magnitude speedup in query execution time over the baseline approaches.

### 3.2 Filter-Verification Query Execution

Without loss of generality, in this section, we will show how MASKSEARCH accelerates the execution of a one-sided filter predicate  $CP(mask, roi, (lv, uv)) > T$ , denoted with  $P$ , as multiple one-sided filter predicates can be combined to form a complex predicate. In §3.3, we will show that our technique applies to accelerating predicates that are in the form of  $CP(\dots) < T$  or involve multiple different CP functions, e.g.,  $CP(\dots) < CP(\dots)$ .

MASKSEARCH takes as input a filter predicate  $P$ , and its goal is to find and return the  $mask\_ids$  of the masks that satisfy  $P$ . At a high level, MASKSEARCH executes the following workflow:

- **Filter stage:** filter out the masks that *are guaranteed to fail* the predicate  $P$ , and add the masks that *are guaranteed to satisfy* the predicate  $P$  directly to the result set, before loading them from disk to memory.
- **Verification stage:** load the remaining unfiltered masks from disk to memory and verify them by applying predicate  $P$ . If a mask satisfies  $P$ , add it to the result set.

**3.2.1 Filter Stage.** At a high level, the algorithm works as follows, for each mask, MASKSEARCH uses the CHI of the mask to compute bounds of  $CP(mask, roi, (lv, uv))$  and it then uses the bounds to determine whether the mask will satisfy  $P$  or not. In this manner, MASKSEARCH reduces the number of masks loaded from disk during the verification stage (§3.2.2) by pruning the masks that are guaranteed to fail  $P$  and adding the masks that are guaranteed to satisfy  $P$  directly to the result set  $R$ . Deriving the bounds of  $CP(mask, roi, (lv, uv))$  is challenging because  $roi$  and  $(lv, uv)$  can be arbitrary and not known in advance. MASKSEARCH addresses this challenge by leveraging the CHI of masks and the (finitely)-additive property of CHI to derive the bounds for arbitrary  $roi$  and  $(lv, uv)$ . **Notation.**  $P$  denotes  $CP(mask, roi, (lv, uv)) > T$ .  $mask$  is uniquely identified by  $mask\_id$ .  $\theta$  denotes the actual value of  $CP(mask, roi, (lv, uv))$ .  $\bar{\theta}$  and  $\theta$  denote the upper bound and the lower bound on  $\theta$  computed by MASKSEARCH, respectively.  $C(mask\_id, r)$  denotes the histogram of reverse cumulative pixel counts of the pixel value bins of region  $r$  in mask  $mask\_id$ , where  $C(mask\_id, r)[i] = CP(mask, r, (p_{min} + i\Delta, p_{max}))$ .

When a session of MASKSEARCH starts, the CHI of each mask is loaded from disk to memory and will be held in memory for the duration of the system run time. In cases where CHI cannot be held in memory, MASKSEARCH loads the CHI of a mask from disk on demand during query execution. Note that the size of the CHI of a mask is much smaller than the size of the mask itself, and therefore, even if the CHI of a mask is on disk, computing the bounds is much less expensive than loading the masks from disk to memory and evaluating the predicate  $P$  on them.

Given a predicate  $P$ , MASKSEARCH processes each mask targeted by the filter predicate in parallel. For each  $mask$  uniquely identified by  $mask\_id$ , MASKSEARCH proceeds as follows:

**Step 1: Compute  $\bar{\theta}$  and  $\theta$ .** In this step, MASKSEARCH computes  $\bar{\theta}$  and  $\theta$  by using the CHI of  $mask\_id$ .

MASKSEARCH uses two approaches to computing two upper bounds,  $\bar{\theta}_1$  and  $\bar{\theta}_2$ , on  $\theta$ , and uses the smaller one as  $\bar{\theta}$ . The first approach identifies the smallest region available in the CHI that covers  $roi$  of  $mask\_id$ , and uses it to compute  $\bar{\theta}_1$ . We denote this region with  $\bar{roi}$ . Then,  $C(mask\_id, \bar{roi})$  can be computed by CHI using Equation (2). Finally,  $\bar{\theta}_1$  is computed as,

$$\bar{\theta}_1 = C(mask\_id, \bar{roi})[\lfloor lv/\Delta \rfloor] - C(mask\_id, \bar{roi})[\lceil uv/\Delta \rceil] \quad (3)$$

where  $\lfloor x \rfloor$  and  $\lceil x \rceil$  denote the floor and ceiling of  $x$ , respectively.

The second approach identifies the largest region covered by  $roi$  available in the CHI for each mask, and uses it to compute  $\bar{\theta}_2$ . We denote this region with  $roi$ . Then,  $C(mask\_id, roi)$  can be computed using Equation (2). Finally,  $\bar{\theta}_2$  is computed as:

$$\bar{\theta}_2 = C(mask\_id, roi)[\lfloor lv/\Delta \rfloor] - C(mask\_id, roi)[\lceil uv/\Delta \rceil] + |roi| - |\bar{roi}| \quad (4)$$

where  $|\cdot|$  denotes the area of a region. Finally,  $\bar{\theta}$  is computed by taking the minimum of  $\bar{\theta}_1$  and  $\bar{\theta}_2$ .

To show  $\bar{\theta}$  is an upper bound of  $\theta$ , we first show the following inequality. Because  $(\lfloor lv/\Delta \rfloor * \Delta, \lceil uv/\Delta \rceil * \Delta)$  is a superset of  $(lv, uv)$ , for any  $mask\_id$  and  $roi$ , we have,

$$C(mask\_id, roi)[\lfloor lv/\Delta \rfloor] - C(mask\_id, roi)[\lceil uv/\Delta \rceil] \geq \theta \quad (5)$$

We now show the following theorem.

**THEOREM 3.2.**  $\bar{\theta}$  is an upper bound of  $\theta$ .

We prove the theorem by showing both  $\bar{\theta}_1 \geq \theta$  and  $\bar{\theta}_2 \geq \theta$ . For conciseness, we omit  $mask\_id$  in  $C(mask\_id, \dots)$  and omit  $mask$  in  $CP(mask, \dots)$  when clear from context, i.e.,  $C(Q)$  denotes  $C(mask\_id, Q)$  and  $CP(Q, (lv, uv))$  denotes  $CP(mask, Q, (lv, uv))$ . We also use  $CP(Q \setminus W, (lv, uv))$  to denote the count of pixels in spatial region  $Q \setminus W$  with pixel values in  $(lv, uv)$ .

**PROOF.** We first show  $\bar{\theta}_1 \geq \theta$ .

$$\bar{\theta}_1 = C(\bar{roi})[\lfloor lv/\Delta \rfloor] - C(\bar{roi})[\lceil uv/\Delta \rceil] \quad (6)$$

$$\geq CP(\bar{roi}, (lv, uv)) \quad (7)$$

$$= CP(roi, (lv, uv)) + CP(\bar{roi} \setminus roi, (lv, uv)) \quad (8)$$

$$\geq CP(roi, (lv, uv)) = \theta \quad (9)$$

where Inequality (7) follows from Equation (5) and Equation (8) follows from the fact that CP is an additive function over disjoint spatial regions.

Let  $L$  denote  $(\lfloor lv/\Delta \rfloor * \Delta, \lceil uv/\Delta \rceil * \Delta)$ . We now show  $\bar{\theta}_2 \geq \theta$ .

$$\theta = CP(roi, (lv, uv)) \quad (10)$$

$$\leq CP(roi, L) \quad (11)$$

$$= CP(\bar{roi}, L) + CP(roi \setminus \bar{roi}, L) \quad (12)$$

$$\leq CP(\bar{roi}, L) + |roi| - |\bar{roi}| \quad (13)$$

$$= C(\bar{roi})[\lfloor lv/\Delta \rfloor] - C(\bar{roi})[\lceil uv/\Delta \rceil] + |roi| - |\bar{roi}| = \bar{\theta}_2 \quad (14)$$

where Equation (12) follows from the fact that CP is an additive function over disjoint spatial regions. Inequality (13) is because the count of pixels in any region with pixel values in any range is bounded by the total number of pixels in the region.  $\square$

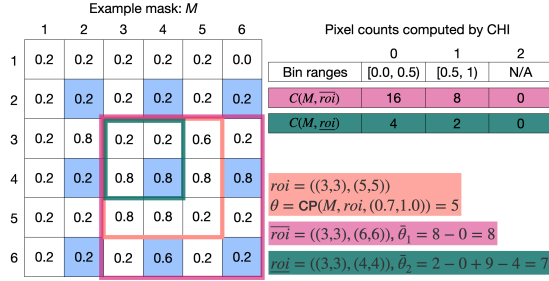


**Figure 4: An example of MASKSEARCH computing the upper bounds,  $\bar{\theta}_1$  and  $\bar{\theta}_2$ , given a mask,  $roi$ , and  $(lv, uv)$ .**

**Example:** The two approaches are illustrated with an example mask in Figure 4. Mask data is the same as in Figure 2. The first approach identifies  $\bar{roi}$ , which is  $((3,3), (6,6))$ , and  $C(M, \bar{roi})$  is computed using Equation (2). Then,  $\bar{\theta}_1$  is computed using Equation (3), i.e.,  $C(M, \bar{roi})[1] - C(M, \bar{roi})[2] = 8 - 0 = 8$ . The second approach identifies  $roi$ , which is  $((3,3), (4,4))$ , and  $C(M, roi)$  is computed using Equation (2). Then,  $\bar{\theta}_2$  is computed using Equation (4), i.e.,  $C(M, roi)[1] - C(M, roi)[2] + |roi| - |\bar{roi}| = 2 - 0 + 9 - 4 = 7$ .

The two approaches are effective in yielding bounds in different scenarios. Intuitively, the first approach is more effective when  $roi$  and  $\bar{roi}$  are close to each other, which would result in a small difference between  $\bar{\theta}_1$  and  $\bar{\theta}$ . The second approach is more effective when  $roi$  and  $\bar{roi}$  are close to each other.

The lower bound,  $\bar{\theta}$ , can be computed similarly following the two approaches. Due to space constraints, we omit the details here.

**Step 2: Determine the relationship between  $\bar{\theta}$  and  $\bar{\theta}$  and  $T$ .** In this step, MASKSEARCH determines whether the predicate  $P$  is satisfied by the mask based on the relationship between  $\bar{\theta}$  and  $\bar{\theta}$  and  $T$ . There are three cases:

- **Case 1:**  $\bar{\theta} \leq T$ . The mask is pruned because it is impossible for the mask to satisfy the predicate  $P$ .
- **Case 2:**  $\bar{\theta} > T$ . The mask is directly added to the result set  $R$  because the mask is guaranteed to satisfy the predicate  $P$ .
- **Case 3:**  $\bar{\theta} \leq T < \bar{\theta}$ . The mask is added to the candidate mask set  $S$  since it needs to be verified against  $P$  in the verification stage.

**3.2.2 Verification Stage.** The verification stage aims to verify each candidate mask in  $S$  that was neither pruned nor directly added to the result set. By loading it from disk and computing the actual value of  $\bar{\theta}$ , and then evaluating the predicate  $P$ , MASKSEARCH determines whether the mask satisfies the predicate  $P$ . If the mask satisfies the predicate  $P$ , it is added to the result set  $R$ .

### 3.3 Generic Predicates

So far, we have described how MASKSEARCH can efficiently process predicates in the form of  $CP(mask, roi, (lv, uv)) > T$ . Supporting predicates in the form of  $CP(mask, roi, (lv, uv)) < T$  is similar to the previous case. The only difference is that in Step 2 of the filter stage, MASKSEARCH directly adds the mask to the result set  $R$  if  $\bar{\theta} < T$  and prunes the mask if  $\bar{\theta} \geq T$ .

MASKSEARCH also supports generic predicates that involve multiple CP functions, i.e.,  $CP_1(\dots) op_1 CP_2(\dots) \dots op_{n-1} CP_n(\dots) > T$ . Let  $F = CP_1(\dots) op_1 CP_2(\dots) \dots op_{n-1} CP_n(\dots)$ . MASKSEARCH uses the lower and upper bounds of every CP function to derive the lower

and upper bounds of  $F$  and use the bounds to efficiently prune the masks that are guaranteed to fail the predicate or guaranteed to satisfy it in the filter stage described in §3.2.1, as long as  $F$  is monotonic with respect to each  $CP_i$  function. Common operators that make  $F$  monotonic include  $+$ ,  $-$ ,  $\times$ .

### 3.4 Aggregation

MASKSEARCH supports queries that contain scalar aggregates on CP functions or on the CP function over mask aggregations, as described in §2. For filter predicates on scalar aggregates, e.g.,  $SUM(CP(mask, roi, (lv, uv))) > T$  group by  $image\_id$ , MASKSEARCH uses the same approach as in §3.3 to efficiently filter out groups of masks associated with the same  $image\_id$  that are guaranteed to fail the predicate or guaranteed to satisfy it, since common scalar aggregate functions (SUM, AVG, and etc.) are monotonic with respect to the CP function. For filter predicates on mask aggregations, e.g.,  $CP(MASK\_AGG(mask), roi, (lv, uv)) > T$ , MASKSEARCH treats the aggregated masks as new masks and uses the same approach described in §3.2 to process the query. The index for the aggregated masks is either built ahead of time or incrementally built (§3.6).

### 3.5 Top-K

To answer top-k queries, MASKSEARCH follows a similar idea as described in §3.2, but it intertwines the filter and verification stages to maintain the current top-k result. Without loss of generality, let's consider the case of a top-K query seeking the masks with the highest values of the CP function. The set of top-k masks can be defined as a set,  $R$ , of  $k$  masks.  $R$  is initially empty and is conceptually built incrementally as the query is executed by identifying and adding to  $R$  the next mask,  $mask$  (associated with its  $CP(mask, roi, (lv, uv))$  value), that satisfies the following condition,

$$CP(mask, roi, (lv, uv)) > \min_{mask' \in R} CP(mask', roi, (lv, uv)) \quad (15)$$

MASKSEARCH sequentially processes the masks. For each mask, it computes the upper bound  $\bar{\theta}$  and compares  $\bar{\theta}$  with the CP values of the current  $R$ . If  $\bar{\theta} \leq \min_{mask' \in R} CP(mask', roi, (lv, uv))$ , the mask is pruned because it is impossible for the mask to be in the top-k result; otherwise, MASKSEARCH loads the mask from disk and computes the actual value of  $CP(mask, roi, (lv, uv))$ . It then updates  $R$  by adding the mask to  $R$  if it satisfies Equation (15).

### 3.6 Incremental Indexing

As we show in §4.2 and §4.3, the vanilla MASKSEARCH system described so far achieves a significant query time improvement over the baselines with a small index size. The approach that vanilla MASKSEARCH uses, however, incurs a potentially high overhead during preprocessing to build the index. Before processing any query, the vanilla MASKSEARCH approach must build the CHI for every mask in the database, which could lead to a long wait time for the user to get the first result.

To address this challenge, we propose building the CHI incrementally as queries are executed so that only the masks that are necessary for the current query are indexed. Every time the user issues a query, as MASKSEARCH sequentially processes each mask as described in §3.2, it checks if the CHI of the mask is already built. If so, MASKSEARCH directly proceeds as described in §3.2. If not,

**Table 1: Summary of evaluated queries based on motivation and related work.**

Query	Description
Q1	Returns masks s.t. $CP(mask, roi, (lv, uv)) > 5000$ , $roi = ((50, 50), (200, 200))$ , $(lv, uv) = (0.6, 1.0)$ , $model\_id = 1$
Q2	Returns masks s.t. $CP(mask, roi, (lv, uv)) > 15,000$ , $roi = \text{object}$ , $(lv, uv) = (0.8, 1.0)$ , $model\_id = 1$
Q3	Returns top-25 masks with largest $CP(mask, roi, (lv, uv))$ , $roi = ((50, 50), (200, 200))$ , $(lv, uv) = (0.8, 1.0)$ , $model\_id = 1$
Q4	Returns top-25 images with largest mean( $CP(mask, roi, (lv, uv))$ ) (groupby $image\_id$ ) for masks associated with two models, $roi = \text{object}$ , $(lv, uv) = (0.8, 1.0)$
Q5	Returns top-25 images with largest $CP(\text{intersect}(mask), roi, (lv, uv))$ (groupby $image\_id$ ) for masks associated with two models, $roi = \text{object}$ , $(lv, uv) = (0.8, 1.0)$

MASKSEARCH executes the query by loading the masks from disk and evaluating whether they satisfy the query predicates. For each mask loaded from disk, MASKSEARCH then builds the CHI for the mask and keeps it in memory for future queries in the same session. When a MASKSEARCH session ends, the CHI for all the masks in the session is persisted to disk for future sessions. With this approach, the cost of building the CHI of a mask is incurred once the first time the mask is loaded from disk, and only if the mask is necessary for a query. In §4.5, we show that MASKSEARCH with such incremental indexing amortizes the cost of indexing quickly and significantly outperforms other baseline methods on multi-query workloads.

## 4 EVALUATION

We implement a prototype of MASKSEARCH in Python and evaluate its performance through experiments on the AWS cloud.

### 4.1 Experimental Setup

**Dataset.** We evaluate MASKSEARCH on two pairs of datasets and models. The first pair of dataset and model, called *WILDS*, is from [37]. *WILDS* contains 22,275 images from the in-distribution (ID) and out-of-distribution (OOD) validation sets of the iWildCam dataset. For each image, we use GradCAM [53] to generate two saliency maps for two different ResNet-50 models trained on the iWildCam training set. Each image in *WILDS*, as well as the saliency map, is  $448 \times 448$  pixels in size. The second pair of dataset and model, called *ImageNet*, contains 1,331,167 images from the ImageNet dataset [50]. We also use GradCAM [53] to generate two saliency maps for two different ResNet-50 models for each image, and use them as the masks for *ImageNet*. Each image and mask in *ImageNet* is  $224 \times 224$  pixels in size. These two pairs of models and datasets complement each other in terms of the number of images (and masks) and the size of the masks.

In terms of MASKSEARCH configuration, we set  $b$  (the number of buckets for pixel value discretization) to 16 for both *WILDS* and *ImageNet*; we also set  $w_c = h_c = 64$  (the cell size for spatial partitioning) for *WILDS* and  $w_c = h_c = 28$  for *ImageNet*, unless otherwise specified. With such index configurations, the uncompressed index size for *ImageNet* is 6.5 GB, which is 4.0% of the compressed size of ImageNet; for *WILDS*, the uncompressed index size is 88 MB, which is 6.5% of the compressed dataset size.

**Baselines.** As discussed in §1 and §5, there is a lack of tooling and system support for the efficient processing of our targeted queries. To the best of our knowledge, no existing system reduces the work required—loading the masks from disk and computing the CP function values for them—to process a query. SciDB [13] is designed to efficiently process large dense arrays, but it is not optimized for efficiently searching through a database of small arrays. Because the community version of SciDB is no longer available, we were unable to include SciDB in our evaluation.

Thus, we compare MASKSEARCH to the following two baselines that must load all masks from disk and process them to answer a query: (1) PostgreSQL 10 (the default version that comes with Ubuntu 18.04). The masks are stored as 2D arrays of floating point numbers in a column as described in §2. The CP function is implemented as a user-defined function (UDF) written in C and compiled into a dynamically shared library. It is loaded by the PostgreSQL server when the CP function is called. (2) NumPy. The masks are stored as NumPy arrays on disk. The CP function is implemented in Python and uses NumPy array functions to ensure vectorized computation.

**Machine configuration.** All experiments were run on an EC2 p3.2xlarge, which has an Intel Xeon E5-2686 v4 processor with 8 vCPUs and 61 GiB of memory, an NVIDIA Tesla V100 GPU with 16 GiB of memory, and EBS gp3 volumes provisioned with 3000 IOPS and 125 MiB/s throughput for disk storage.

### 4.2 Individual Query Performance

We first evaluate the performance of MASKSEARCH on 5 individual queries motivated by the use cases in §1 and §2:

- Q1 (Filter): mask selection query with a filter predicate on CP with a constant  $roi$  across all masks. This query corresponds to the query in the chest X-ray example in §1.
- Q2 (Filter): mask selection query with a filter predicate on CP with different  $rois$  for different masks. This query is a variant of Q1 with the difference in  $roi$  specification.
- Q3 (Top-K): top- $k$  mask selection query, ranked by CP with a constant  $roi$  across all masks. This query corresponds to the query in Example 1 in §2.
- Q4 (Aggregation): image selection query with an aggregation over the CP values of masks associated with different models (SCALAR\_AGG in §2.2), with a filter predicate on the aggregated values. This query is a variant of the query in Example 2 in §2.
- Q5 (Mask Aggregation): image selection query with a filter predicate on the CP value of the aggregated mask computed from the masks associated with different models (MASK\_AGG in §2.2). This query corresponds to the query in Example 2 in §2.

The specific parameters for each query are shown in Table 1. When  $roi$  is set to object, the  $roi$  is the bounding box of the foreground object in the image generated by YOLOv5 [33]. We build the CHI for all masks prior to executing the benchmark queries and clear the OS page cache before each query execution. The median execution time of 5 runs for each query is shown in Figure 5. In addition, Table 2 displays the number of masks loaded from disk by each system during query execution.

As the figure shows, on *WILDS*, it takes NumPy and PostgreSQL around 2 minutes to answer each query; on *ImageNet*, it takes them more than 30 minutes to answer each query. On the same dataset,

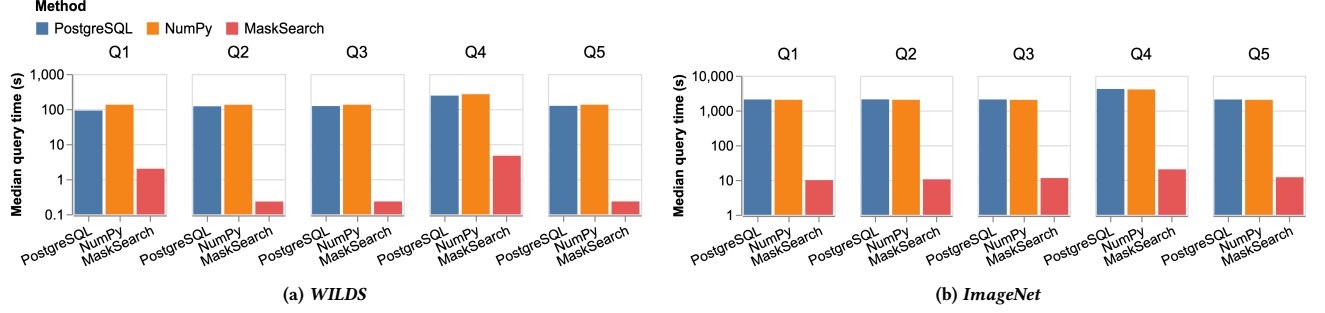


Figure 5: End-to-end individual query execution time based on motivation and related work. The index size for MASKSEARCH is  $\sim 5\%$  of the original dataset size for both datasets. Note the log scale on the y-axis.

Table 2: Number of masks loaded during query execution. NP = NumPy, PG = PostgreSQL.

Dataset	Method	Q1	Q2	Q3	Q4	Q5
WILDS	MASKSEARCH	407	40	32	874	48
	NP & PG	22,275	22,275	22,275	44,550	22,275
ImageNet	MASKSEARCH	2696	3849	2943	1494	2768
	NP & PG	1,331,167	1,331,167	1,331,167	2,662,334	1,331,167

the performance of NumPy and PostgreSQL is similar across all queries because they both load all masks from disk and process them to generate the query results. The execution time for Q4 is longer than other queries because it requires loading two masks for each image since it contains an aggregation over the CP values of such masks. During query execution by NumPy and PostgreSQL, we also observed that the disk read bandwidth is saturated, i.e., it reaches 125 MiB/s, which is the provisioned disk read bandwidth for our EBS volumes. This confirms that the query execution time is dominated by the time required to load the masks from disk. Therefore, any system that does not reduce the number of masks loaded from disk during query execution can achieve, at best, a comparable query execution time to that of NumPy and PostgreSQL.

MASKSEARCH executes each query in under 5 seconds on *WILDS* and in less than 20 seconds on *ImageNet*, providing query time speedups of up to two orders of magnitude over both baselines. This significant difference in performance is attributed to MASKSEARCH loading many fewer masks (shown in Table 2) because its filter-verification framework enables it to avoid loading from disk the masks that are guaranteed to satisfy the query predicate or guaranteed to fail it. On *ImageNet*, MASKSEARCH’s query time for Q4 is longer compared to other queries, even though the number of masks loaded for Q4 is smaller. This discrepancy stems from the additional computation MASKSEARCH performs for Q4 ( $2\times$  bound computation than other queries), as it contains an aggregation.

### 4.3 Performance on Different Query Types

In this experiment, we evaluate the performance of MASKSEARCH on three types of queries with varying parameters. We only show the execution times of MASKSEARCH because, for each query type, baseline methods have similar execution times as the queries of the same type in §4.2, regardless of specific query parameters. For each dataset and query type, we generate 500 queries with randomized parameters and execute them using MASKSEARCH:

- **Filter:** this query type contains mask selection queries with a filter predicate  $CP(mask, roi, (lv, uv)) > T$ . For every query,

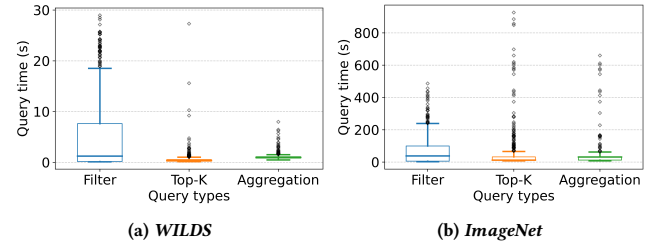


Figure 6: Query time of MASKSEARCH for different query types. Index size for MASKSEARCH:  $\sim 5\%$  of dataset size.

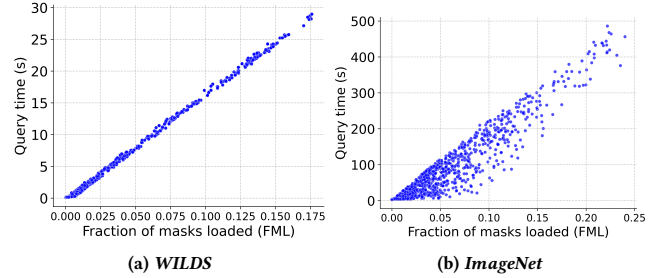


Figure 7: The relationship between end-to-end query time and the fraction of masks loaded (FML) for a query.

$roi$  is set as the foreground object bounding box in a mask generated by YOLOv5 [33].  $lv$  and  $uv$  are randomly selected from  $[0.1, \dots, 0.9]$  and  $uv$  is always greater than  $lv$ . The count threshold  $T$  is randomly chosen from  $[0, 1, \dots, \text{total \# pixels}]$ .

- **Top-K:** this query type returns masks ranked by  $CP(mask, roi, (lv, uv))$ . For each query,  $roi$  is randomly generated as any rectangle within the masks. This  $roi$  is generated once for each query and remains constant across all masks.  $k$  is set to 25. The order of query result, i.e., ORDER BY ... DESC or ASC, is randomly selected for each query.
- **Aggregation:** this type of query returns images ranked by  $\text{mean}(CP(mask, roi, (lv, uv)))$  of multiple masks associated with each image. Two masks are associated with each image and they are generated by GradCAM based on different models.  $k$  is set to 25.  $roi$ ,  $lv$ ,  $uv$ , and the order of the query result is randomly selected for each query.

Figure 6 shows the distribution of query execution times for each query type on both *WILDS* and *ImageNet*. The figure displays the median, minimum, maximum, and interquartile range (IQR) of



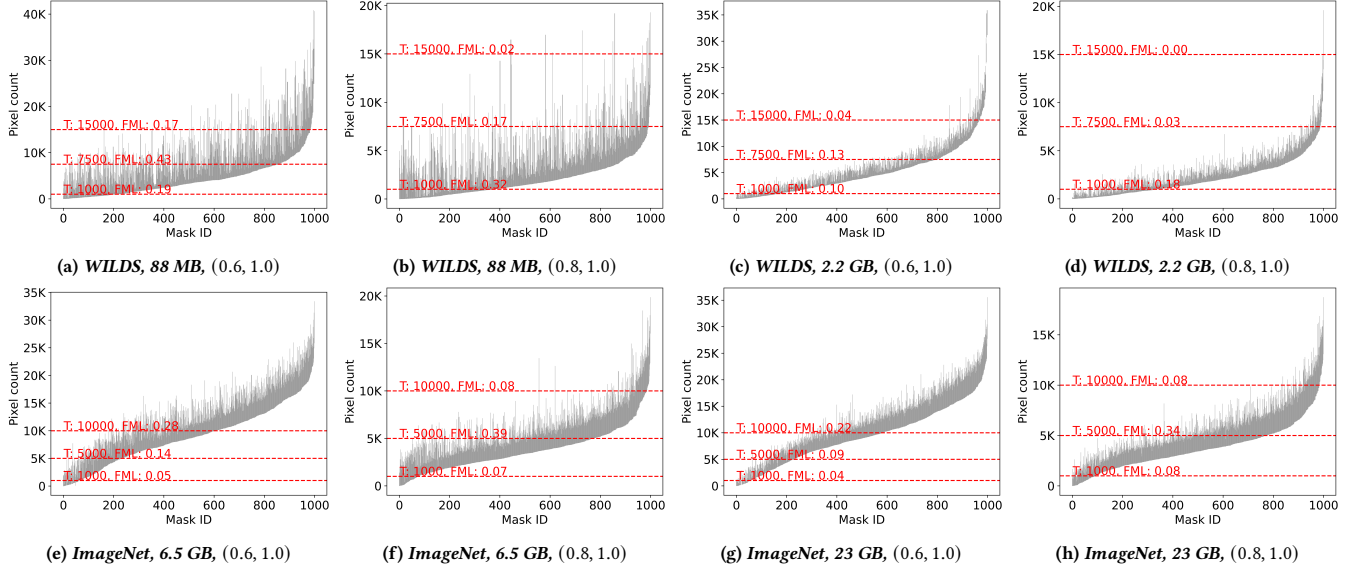


**Figure 8: Distribution of bounds of  $CP(mask, roi, (lv, uv))$  computed by MASKSEARCH.** Each subfigure represents the distribution for a combination of (dataset, index size,  $(lv, uv)$ ), shown as the title of each. Each vertical segment represents the lower and upper bounds of  $CP(mask, roi, (lv, uv))$  for a single mask. For each mask,  $roi$  is the foreground object bounding box. We show the distribution of bounds for 1000 randomly sampled masks in each subplot. The x-axes represent the masks sorted by their lower bounds. The horizontal dashed lines represent examples of the count threshold  $T$ . FML is the fraction of masks loaded by MASKSEARCH given a predicate  $CP(mask, roi, (lv, uv)) > T$ . For each count threshold  $T$ , FML is equal to the fraction of the vertical segments that intersect with the horizontal dashed line defined by  $T$ . Note the different scales of the y-axes.

these times. The whiskers represent outliers, which are defined as values that are more than 1.5 times the IQR away from the median.

MASKSEARCH demonstrates its superior query execution performance across all query types with varying parameters. Even when considering the worst-case execution time (i.e., the outliers), MASKSEARCH would still outperform the baselines by a considerable margin, because the baselines would still load all masks from disk and process them, regardless of the query parameters.

Moreover, we find that the query execution times of MASKSEARCH do not exhibit a strong correlation across different query types. We note that the 75th percentile of the *Filter* query type has a longer execution time than that of the other two query types. This is because, for the other query types, MASKSEARCH compares the bounds (of CP) with the CP values of the current top- $k$  set ( $k=25$ ). This process generally allows for more efficient mask filtering than comparing the bounds with a fixed count threshold  $T$  in the *Filter* query type. For example, on *WILDS*, at the 75th percentile in query time, the number of masks pruned in MASKSEARCH’s filter stage during query execution is 21,184 for the *Filter* query type, 22,106 for *Top-K*, 21,677 for *Aggregation*.

Instead, we observe that the execution times tend to differ more significantly among queries with different parameters within the same query type. In fact, as we discuss further in §4.4, for a given dataset, the query execution time of MASKSEARCH is primarily determined by the fraction of masks loaded (FML), i.e., masks that are loaded from disk and used to compute its CP value during query execution. The difference in execution times within the same query type is mainly due to the difference in the FML for each query. For

example, for the *Filter* query type on *WILDS*, the FML at the 25th, 50th, and 75th percentiles are 0.002, 0.012, and 0.049, respectively.

#### 4.4 MASKSEARCH’s Query Time Analysis

In this section, we explore factors affecting MASKSEARCH’s query execution time by analyzing 1500 *Filter* queries, defined in §4.3, executed by MASKSEARCH on each dataset.

With Figure 7, we first establish that, given a dataset, MASKSEARCH’s query execution time is proportional to the fraction of masks loaded (FML) for each query. The FML for a query is defined as the ratio of masks loaded from disk and used to compute their actual CP values to the total number of masks in a dataset. The correlation coefficient between query time and FML is 0.99 for *WILDS* and 0.96 for *ImageNet*. It again corroborates that query execution time is dominated by loading masks from disk and computing their CP values, with a higher FML indicating more masks being loaded from disk.

Now that we have established the relationship between query execution time and FML, we investigate the factors that affect FML, including the query parameters (region of interest  $roi$ , pixel value range  $(lv, uv)$ , count threshold  $T$ ), data in the masks ( $mask$ ), and index granularity (index size). For MASKSEARCH, FML is the fraction of masks that are neither pruned nor added directly to the result set by the filter stage in the filter-verification framework. FML corresponds to *Case 3* in Step 2 of the filter stage; for each mask belonging to this case, its lower bound  $\underline{\theta}$  for CP computed by MASKSEARCH is not greater than the count threshold  $T$  and its upper bound  $\bar{\theta}$  for CP is greater than  $T$ , i.e.,  $\underline{\theta} \leq T < \bar{\theta}$ .



Figure 8 shows the distribution of bounds computed by MASKSEARCH for both datasets and queries with varying parameters from the 1500 *Filter* queries analyzed. Each subfigure shows the distribution of bounds for a different (dataset, index size,  $(lv, uv)$ ) combination. The *roi* for all subfigures is the foreground object bounding box. The (vertical) segments in each subfigure represent the bounds computed by MASKSEARCH for 1000 masks randomly sampled from the dataset. Each red horizontal dashed line represents an example count threshold  $T$ . In this way, each subfigure visualizes the relationship between the bounds and FML: for each count threshold  $T$ , FML equals the fraction of the segments intersecting with the red dashed line defined by  $T$ .

In each subfigure, different count thresholds  $T$  lead to varying FMLs for the same dataset, index size, and query parameters, as the fraction of segments intersecting with the red dashed line changes.

Comparing subfigures with the same *roi* and  $(lv, uv)$  but on different datasets reveals that different sets of masks can result in different FMLs for the same query parameters because of different pixel value distributions in the *roi* of the masks. Similarly, changing *roi* essentially alters the set of masks targeted by the query, leading to different FMLs. Subfigures with the same dataset and *roi* but different  $(lv, uv)$  configurations also exhibit different bound distributions and FMLs for the same count threshold  $T$ .

Moreover, subfigures sharing the same dataset and  $(lv, uv)$  but with varying index sizes display different bound distributions and FMLs as well. Larger index sizes offer more granular indexes, tighter bounds (shorter vertical segments in the figure), and lower FMLs for the same query parameters. For example, comparing Figure 8 (a) and (c), we observe that the bounds computed by MASKSEARCH for *WILDS* with  $(lv, uv) = (0.6, 1.0)$  are tighter for the larger index size. Therefore, the FML for the same count threshold  $T$  is lower for the larger index size.

In conclusion, the data in the masks, region of interest *roi*, pixel value range  $(lv, uv)$ , and index size determine the distribution of bounds computed by MASKSEARCH. The count threshold  $T$  defines the FML given the distribution of bounds, and the FML dictates the query execution time of MASKSEARCH. The granularity of the index represents a trade-off between index size and query time, depending on user application requirements and available resources.

## 4.5 Multi-Query Workload Performance

In this section, we evaluate MASKSEARCH on multi-query workloads with and without the incremental indexing technique (§3.6) which mitigates MASKSEARCH’s potential start-up overheads. We generate workloads to simulate the exploration and analysis processes of users who seek to identify sets of masks satisfying a given predicate.

We simulate workloads where a user begins with a query targeting masks of image subsets belonging to certain classes and then progressively explores masks associated with other classes. For example, to identify images with spurious correlations (§2.1), the user may first look at the confusion matrix and identify classes with high false positive rates. Then, the user may issue queries to retrieve images predicted as those classes to identify possible spurious correlations. Several queries may be issued targeting those masks, as different query parameters (e.g., *roi*,  $lv$ ,  $uv$ ,  $T$ ) may be used to retrieve and rank masks with different properties, e.g.,

masks focusing on the foreground object and masks focusing on the background. After analyzing the returned masks, the user may continue to explore masks of other classes and repeat the process.

To account for this behavior, we generate four different workloads for each dataset, each of which comprises 200 *Filter* queries, with query parameters randomly generated following the approach described in §4.3. A parameter  $p_{seen}$  is associated with each workload, representing the likelihood of querying previously targeted masks within the same workload. Randomized query parameters and  $p_{seen}$  are intended to simulate the user’s behavior of issuing multiple queries targeting the same set of masks with different parameters to retrieve masks having different properties. Additionally, each query within a workload targets a specific subset of masks (e.g., masks of images predicted as certain classes) from the corresponding full dataset. Let  $N$  denote the total number of masks within a dataset. The number of masks targeted by each query,  $n$ , is randomly chosen from  $[0.1 \cdot N, 0.2 \cdot N, 0.3 \cdot N]$ . Then, the set of targeted masks are generated as follows, we sample without replacement  $n$  masks consisting of  $p_{seen}\%$  targeted masks and  $(1 - p_{seen})\%$  unseen ones. Note that when the number of remaining unseen masks is less than  $n \cdot (1 - p_{seen})$ , we include all the unseen masks in the current query and switch to only sampling seen masks for the remaining queries in the workload.

The workloads are labeled as Workload 1, 2, 3, and 4, with their respective  $p_{seen}$  values set to 0.2, 0.5, 0.8, and 1.0. These probabilities signify varying levels of dataset exploration, with Workload 1 exhibiting the highest degree of exploration and Workload 4 exhibiting the lowest. By evaluating MASKSEARCH’s performance across these diverse workloads, we aim to assess its effectiveness under a range of dataset exploration scenarios.

Figure 9 shows the performance of MASKSEARCH on these four workloads for both *WILDS* and *ImageNet*. MASKSEARCH is evaluated with and without incremental indexing against NumPy which represents existing methods that must load and process all masks from disk for each query. In the figure, MS-II refers to MASKSEARCH with incremental indexing and MS refers to MASKSEARCH without incremental indexing. We measure the cumulative total time, i.e., the time elapsed for index building plus the time elapsed for query execution, for each method. Figure 9 shows the result. Note that the time to initially build the indexes without incremental indexing is included with the 0-th query for MS in all subfigures.

Figure 9 (a) and (b) show the cumulative total times for Workload 2. The results for other workloads are not shown because MS and NumPy have similar performance trends across all workloads. MS exhibits a slow growth in cumulative total time because it executes all queries efficiently with the filter-verification query processing framework. However, it incurs a start-up overhead due to the need to build indexes for all masks in the dataset ahead of time. In contrast, NumPy has no start-up overhead but suffers from a rapid growth in its cumulative time because it does not reduce the required work for each query. Nevertheless, the cost of building the indexes for MS is quickly amortized across the queries thanks to the filter-verification query processing framework and the CHI technique. On both datasets, MS outperforms NumPy after approximately 10 queries. MS-II strikes a good balance between MS and NumPy, eliminating the start-up overhead while achieving comparable query execution times to MS.

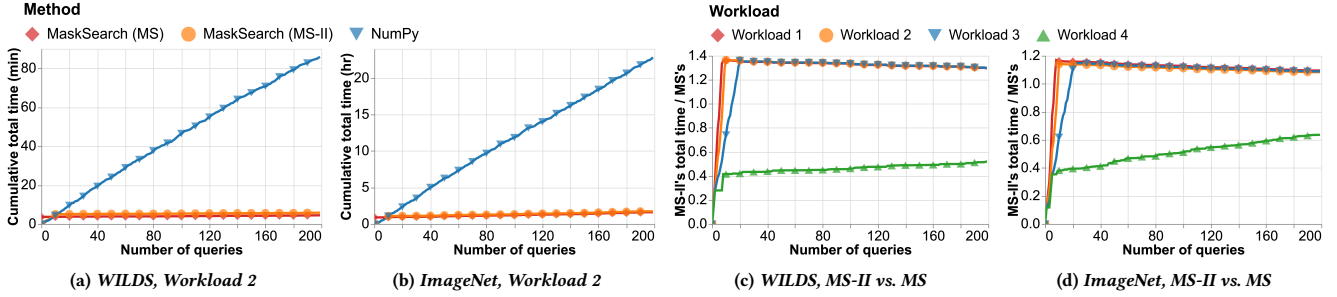


**Figure 9: Cumulative total time, incl. index building time and query time, for multi-query workloads. MS-II and MS refer to MASKSEARCH w/ and w/o incremental indexing, respectively. (a) and (b) show the total time for MS, MS-II, and NumPy for Workload 2; (c) and (d) show the ratio of the cumulative total time of MS-II to that of MS for all workloads. The index size for MS is  $\sim 5\%$  of the corresponding dataset. MS-II builds the index incrementally using the same index configuration as MS.**

Figure 9 (c) and (d) show the ratio of cumulative total time between MS-II and MS for all workloads on both datasets. We first discuss the results for Workload 1, 2, and 3. For both datasets, we observe that this ratio grows rapidly at the beginning for Workload 1, 2, and 3, and then peaks at around 10 to 20 queries before decreasing gradually. The initial fast growth is due to the fact that for the first few queries, MS-II needs to answer them without the help of indexes for the unseen masks targeted, which is similar to the behavior of NumPy, and to build indexes for these masks. Among workloads, Workload 1 has the highest growth rate in this ratio because it has the lowest  $p_{seen}$  value, resulting in more unseen masks being targeted during the first few queries and therefore forcing MS-II to build indexes for more masks. Then, the ratio peaks at around 10 to 20 queries because, at this point, MS-II has built indexes for all the masks in the dataset, and subsequent queries can be executed using the filter-verification framework without index building. The peak ratio exceeds 1.0 because MS-II must load the masks from disk and compute their CP values during query execution the first time they are targeted. In contrast, MS utilizes pre-built indexes for all targeted masks in all queries, which results in a lower cumulative total time. Then, after the peak, the ratio decreases gradually because the cumulative total time for MS-II grows at a similar rate to MS’s cumulative total time.

For Workload 4, on both datasets, MS-II never completes building the indexes for all masks, as only 30% of the masks in the dataset (6683 for *WILDS* and 399,351 for *ImageNet*) are eventually targeted by all the queries in this workload. As a result, after the rapid initial growth, the ratio of cumulative total time plateaus. This ratio never reaches 1.0 because the time spent by MS to build the indexes for the never-targeted masks is not amortized across queries.

Lastly, we note that users typically pause between queries to examine the query results. Hence, MASKSEARCH can leverage that time to compute the indexes, which would yield better user-perceived latencies for query results.

## 5 RELATED WORK

**Masks in ML.** Masks are widely used in ML to annotate image content, e.g., saliency maps [53, 55, 56, 65] and segmentation maps [27, 36, 49]. Practitioners use them for a variety of applications,

including identifying maliciously attacked examples [59, 63, 64], detecting out-of-distribution examples [30], monitoring model errors [1, 3, 35], and performing traffic and retail analytics [2, 4]. These applications motivate the design of MASKSEARCH and could utilize MASKSEARCH’s efficient query execution to quickly retrieve examples that satisfy the desired properties.

**Data systems for ML workloads and queries.** Numerous systems have been proposed to better support ML workloads and queries [7, 12, 19, 21, 26, 41, 45, 58, 62]. MASKSEARCH is related to systems that support the inspection, explanation, and debugging of ML models [24, 25, 40, 52, 57, 61]. Among these, DeepEverest [24] is the closest to MASKSEARCH. It is designed to support the efficient retrieval of examples based on neural representations, helping users better understand neural network behavior. While MASKSEARCH also focuses on efficiently retrieving examples, it targets queries based on mask properties rather than neural representations.

**Image databases and querying.** Many systems and techniques support efficient queries over image databases [8, 10, 20, 47, 51]. However, these methods are not optimized for our target queries. For example, VDMS [47] focuses on retrieving images based on metadata, while DeepLake [23] supports content-based queries but lacks support for querying based on aggregations over pixels. Array databases like SciDB [13] are designed for handling multi-dimensional dense arrays but do not efficiently support searching through large numbers of arrays. In contrast to MASKSEARCH, these existing systems do not reduce the work required to execute our target queries. Moreover, existing multi-dimensional indexes, discussed in §2.3, are ill-suited for dense data like masks and fail to accommodate mask-specific regions of interest in queries.

## 6 CONCLUSION

We introduced MASKSEARCH, a system that accelerates queries that retrieve examples based on mask properties. By leveraging a novel indexing technique and an efficient filter-verification execution framework, MASKSEARCH significantly reduces the masks that must be loaded from disk during query execution. With around 5% of the size of the dataset, MASKSEARCH accelerates individual queries by two orders of magnitude and consistently outperforms existing methods on various multi-query workloads.

## REFERENCES

- [1] [n.d.]. Meerkat and the Path to Foundation Models as a Reliable Software Abstraction. <https://hazyresearch.stanford.edu/blog/2023-03-01-meerkat>. Accessed: 2023-04-20.
- [2] [n.d.]. Retail - DataFromSky. <https://datafromsky.com/retail/>. Accessed: 2023-04-20.
- [3] [n.d.]. TESLA'S DATA ENGINE AND WHAT WE SHOULD LEARN FROM IT. <https://www.braincreators.com/insights/teslas-data-engine-and-what-we-should-all-learn-from-it>. Accessed: 2023-04-20.
- [4] [n.d.]. Traffic Monitoring - DataFromSky. <https://datafromsky.com/traffic-monitoring/>. Accessed: 2023-04-20.
- [5] Firas Abuzaid, Peter Bailis, Jialin Ding, Edward Gan, Samuel Madden, Deepak Narayanan, Kexin Rong, and Sahaana Suri. 2018. MacroBase: Prioritizing Attention in Fast Data. *ACM Trans. Database Syst.* 43, 4, Article 15 (dec 2018), 45 pages. <https://doi.org/10.1145/3276463>
- [6] Michael R. Anderson, Michael J. Cafarella, Germán Ros, and Thomas F. Wenisch. 2018. Physical Representation-based Predicate Optimization for a Visual Analytics Database. *CoRR abs/1806.04226* (2018). arXiv:1806.04226 <http://arxiv.org/abs/1806.04226>
- [7] Yuki Asada, Victor Fu, Apurva Gandhi, Advitya Gemawat, Lihao Zhang, Dong He, Vivek Gupta, Ehi Nosakhare, Dalitso Banda, Rathijit Sen, and Matteo Interlandi. 2022. Share the Tensor Tea: How Databases Can Leverage the Machine Learning Ecosystem. *Proc. VLDB Endow.* 15, 12 (aug 2022), 3598–3601. <https://doi.org/10.14778/3554821.3554853>
- [8] Doug Beaver, Sanjeev Kumar, Harry C Li, Jason Sobel, Peter Vajgel, et al. 2010. Finding a Needle in Haystack: Facebook's Photo Storage.. In *OSDI*, Vol. 10. 1–8.
- [9] Deblina Bhattacharjee, Martin Everaert, Mathieu Salzmann, and Sabine Süsstrunk. 2022. Estimating Image Depth in the Comics Domain. In *Proceedings of the IEEE/CVF Winter Conference on Applications of Computer Vision (WACV)*. 2070–2079.
- [10] Avinash N Bhute and BB Meshram. 2014. Content based image indexing and retrieval. *arXiv preprint arXiv:1401.1742* (2014).
- [11] Alceu Bissoto, Michel Fornaciari, Eduardo Valle, and Sandra Avila. 2019. (De) Constructing bias on skin lesion datasets. In *Proceedings of the IEEE/CVF Conference on Computer Vision and Pattern Recognition Workshops*. 0–0.
- [12] Matthias Boehm, Iulian Antonov, Sebastian Baunsgaard, Mark Dokter, Robert Ginthör, Kevin Innerebner, Florijan Klezin, Stefanie Lindstaedt, Arnab Phani, Benjamin Rath, et al. 2019. SystemDS: A declarative machine learning system for the end-to-end data science lifecycle. *arXiv preprint arXiv:1909.02976* (2019).
- [13] Paul G. Brown. 2010. Overview of SciDB: Large Scale Array Storage, Processing and Analysis. In *Proceedings of the 2010 ACM SIGMOD International Conference on Management of Data* (Indianapolis, Indiana, USA) (*SIGMOD '10*). Association for Computing Machinery, New York, NY, USA, 963–968. <https://doi.org/10.1145/1807167.1807271>
- [14] Z. Cao, G. Hidalgo Martinez, T. Simon, S. Wei, and Y. A. Sheikh. 2019. OpenPose: Realtime Multi-Person 2D Pose Estimation using Part Affinity Fields. *IEEE Transactions on Pattern Analysis and Machine Intelligence* (2019).
- [15] Bernard Chazelle. 1990. Lower Bounds for Orthogonal Range Searching: I. The Reporting Case. *J. ACM* 37, 2 (apr 1990), 200–212. <https://doi.org/10.1145/77600.77614>
- [16] Bernard Chazelle. 1990. Lower Bounds for Orthogonal Range Searching: I. The Reporting Case. *J. ACM* 37, 2 (apr 1990), 200–212. <https://doi.org/10.1145/77600.77614>
- [17] Abhishek Das, Harsh Agrawal, C. Lawrence Zitnick, Devi Parikh, and Dhruv Batra. 2016. Human Attention in Visual Question Answering: Do Humans and Deep Networks Look at the Same Regions? arXiv:1606.03556 [cs.CV]
- [18] Alex J DeGrave, Joseph D Janizek, and Su-In Lee. 2021. AI for radiographic COVID-19 detection selects shortcuts over signal. *Nature Machine Intelligence* 3, 7 (2021), 610–619.
- [19] Francesco Del Buono, Matteo Paganelli, Paolo Sottovia, Matteo Interlandi, and Francesco Guerra. 2021. Transforming ML Predictive Pipelines into SQL with MASQ. In *Proceedings of the 2021 International Conference on Management of Data* (Virtual Event, China) (*SIGMOD '21*). Association for Computing Machinery, New York, NY, USA, 2696–2700. <https://doi.org/10.1145/3448016.3452771>
- [20] M. Flickner, H. Sawhney, W. Niblack, J. Ashley, Qian Huang, B. Dom, M. Gorkani, J. Hafner, D. Lee, D. Petkovic, D. Steele, and P. Yanker. 1995. Query by image and video content: the QBIC system. *Computer* 28, 9 (1995), 23–32. <https://doi.org/10.1109/2.410146>
- [21] Gharib Gharibi, Vijay Walunj, Rakan Alanazi, Sirisha Rella, and Yuyang Lee. 2019. Automated management of deep learning experiments. In *Proceedings of the 3rd International Workshop on Data Management for End-to-End Machine Learning*. 1–4.
- [22] Riza Alp Güler, Natalia Neverova, and Iasonas Kokkinos. 2018. Densepose: Dense human pose estimation in the wild. In *Proceedings of the IEEE conference on computer vision and pattern recognition*. 7297–7306.
- [23] Sasun Hambardzumyan, Abhinav Tuli, Levon Ghukasyan, Fariz Rahman, Hrant Topchyan, David Isayan, Mark McQuade, Mikayel Harutyunyan, Tatevik Hakobyan, Ivo Stranic, and Davit Buniatyan. 2022. Deep Lake: a Lakehouse for Deep Learning. arXiv:2209.10785 [cs.DC]
- [24] Dong He, Maureen Daum, Walter Cai, and Magdalena Balazinska. 2021. DeepEverest: Accelerating Declarative Top-K Queries for Deep Neural Network Interpretation. *Proc. VLDB Endow.* 15, 1 (sep 2021), 98–111. <https://doi.org/10.14778/3485450.3485460>
- [25] Dong He, Maureen Daum, Walter Cai, and Magdalena Balazinska. 2021. DeepEverest: Accelerating Declarative Top-K Queries for Deep Neural Network Interpretation [Technical Report]. *arXiv preprint arXiv:2104.02234* (2021).
- [26] Dong He, Supun C Nakandala, Dalitso Banda, Rathijit Sen, Karla Saur, Kwanghyun Park, Carlo Curino, Jesús Camacho-Rodríguez, Konstantinos Karanasos, and Matteo Interlandi. 2022. Query Processing on Tensor Computation Runtimes. *Proc. VLDB Endow.* 15, 11 (sep 2022), 2811–2825. <https://doi.org/10.14778/3551793.3551833>
- [27] Kaiming He, Georgia Gkioxari, Piotr Dollár, and Ross Girshick. 2018. Mask R-CNN. arXiv:1703.06870 [cs.CV]
- [28] Kaiming He, Xiangyu Zhang, Shaoqing Ren, and Jian Sun. 2016. Deep residual learning for image recognition. In *Proceedings of the IEEE conference on computer vision and pattern recognition*. 770–778.
- [29] Sungsoo Ray Hong, Jessica Hullman, and Enrico Bertini. 2020. Human factors in model interpretability: Industry practices, challenges, and needs. *Proceedings of the ACM on Human-Computer Interaction* 4, CSCW1 (2020), 1–26.
- [30] Julia Hornauer and Vasileios Belagiannis. 2022. Heatmap-based Out-of-Distribution Detection. arXiv:2211.08115 [cs.CV]
- [31] Kevin Hsieh, Ganesh Ananthanarayanan, Peter Bodik, Shivaram Venkataraman, Paramvir Bahl, Matthai Philipose, Phillip B. Gibbons, and Onur Mutlu. 2018. Focus: Querying Large Video Datasets with Low Latency and Low Cost. In *13th USENIX Symposium on Operating Systems Design and Implementation (OSDI 18)*. USENIX Association, Carlsbad, CA, 269–286. <https://www.usenix.org/conference/osdi18/presentation/hsieh>
- [32] Yu Jiang, Guoliang Li, Jianhua Feng, and Wen-Syan Li. 2014. String Similarity Joins: An Experimental Evaluation. *Proc. VLDB Endow.* 7, 8 (apr 2014), 625–636. <https://doi.org/10.14778/2732296.2732299>
- [33] Glenn Jocher. 2020. YOLOv5 by Ultralytics. <https://doi.org/10.5281/zenodo.3908559>
- [34] Daniel Kang, John Emmons, Firas Abuzaid, Peter Bailis, and Matei Zaharia. 2017. NoScope: Optimizing Neural Network Queries over Video at Scale. *Proc. VLDB Endow.* 10, 11 (aug 2017), 1586–1597. <https://doi.org/10.14778/3137628.3137664>
- [35] DANIEL KANG, JOHN GUIBAS, PETER BAILIS, TATSUNORI HASHIMOTO, YI SUN, and MATEI ZAHARIA. [n.d.]. Data Management for ML-based Analytics and Beyond. ([n.d.]).
- [36] Alexander Kirillov, Eric Mintun, Nikhila Ravi, Hanzi Mao, Chloe Rolland, Laura Gustafson, Tete Xiao, Spencer Whitehead, Alexander C. Berg, Wan-Yen Lo, Piotr Dollár, and Ross Girshick. 2023. Segment Anything. arXiv:2304.02643 [cs.CV]
- [37] Pang Wei Koh, Shiori Sagawa, Henrik Marklund, Sang Michael Xie, Marvin Zhang, Akshay Balsubramani, Weihua Hu, Michihiro Yasunaga, Richard Lanús Phillips, Sara Beery, Jure Leskovec, Anshul Kundaje, Emma Pierson, Sergey Levine, Chelsea Finn, and Percy Liang. 2020. WILDS: A Benchmark of in-the-Wild Distribution Shifts. *CoRR abs/2012.07421* (2020). arXiv:2012.07421 <https://arxiv.org/abs/2012.07421>
- [38] Yao Lu, Aakanksha Chowdhery, Srikanth Kandula, and Surajit Chaudhuri. 2018. Accelerating Machine Learning Inference with Probabilistic Predicates. In *Proceedings of the 2018 International Conference on Management of Data* (Houston, TX, USA) (*SIGMOD '18*). Association for Computing Machinery, New York, NY, USA, 1493–1508. <https://doi.org/10.1145/3183713.3183751>
- [39] Willi Mann, Nikolaus Augsten, and Panagiotis Boursos. 2016. An Empirical Evaluation of Set Similarity Join Techniques. *Proc. VLDB Endow.* 9, 9 (may 2016), 636–647. <https://doi.org/10.14778/2947618.2947620>
- [40] Parmita Mehta, Stephen Portillo, Magdalena Balazinska, and Andrew Connolly. 2020. Toward Sampling for Deep Learning Model Diagnosis. In *2020 IEEE 36th International Conference on Data Engineering (ICDE)*. IEEE, 1910–1913.
- [41] Hui Miao, Ang Li, Larry S Davis, and Amol Deshpande. 2017. Modelhub: Deep learning lifecycle management. In *2017 IEEE 33rd International Conference on Data Engineering (ICDE)*. IEEE, 1393–1394.
- [42] Yifei Ming, Hang Yin, and Yixuan Li. 2021. On the Impact of Spurious Correlation for Out-of-distribution Detection. arXiv:2109.05642 [cs.LG]
- [43] Luke Oakden-Rayner, Jared Dunnmon, Gustavo Carneiro, and Christopher Ré. 2020. Hidden stratification causes clinically meaningful failures in machine learning for medical imaging. In *Proceedings of the ACM conference on health, inference, and learning*. 151–159.
- [44] Vaishakh Patil, Christos Sakaridis, Alex Liniger, and Luc Van Gool. 2022. P3Depth: Monocular Depth Estimation with a Piecewise Planarity Prior. In *Proceedings of the IEEE/CVF Conference on Computer Vision and Pattern Recognition (CVPR)*.
- [45] Arnab Phani, Benjamin Rath, and Matthias Boehm. 2021. LIMA: Fine-grained Lineage Tracing and Reuse in Machine Learning Systems. In *Proceedings of the 2021 International Conference on Management of Data*. 1426–1439.
- [46] Gregory Plumb, Marco Tulio Ribeiro, and Ameet Talwalkar. 2022. Finding and Fixing Spurious Patterns with Explanations. arXiv:2106.02112 [cs.LG]

- [47] Luis Remis and Chaunté W. Lacewell. 2021. Using VDMS to Index and Search 100M Images. *Proc. VLDB Endow.* 14, 12 (jul 2021), 3240–3252. <https://doi.org/10.14778/3476311.3476381>
- [48] Marco Tulio Ribeiro, Sameer Singh, and Carlos Guestrin. 2016. "Why should i trust you?" Explaining the predictions of any classifier. In *Proceedings of the 22nd ACM SIGKDD international conference on knowledge discovery and data mining*. 1135–1144.
- [49] Olaf Ronneberger, Philipp Fischer, and Thomas Brox. 2015. U-Net: Convolutional Networks for Biomedical Image Segmentation. [arXiv:1505.04597 \[cs.CV\]](https://arxiv.org/abs/1505.04597)
- [50] Olga Russakovsky, Jia Deng, Hao Su, Jonathan Krause, Sanjeev Satheesh, Sean Ma, Zhiheng Huang, Andrej Karpathy, Aditya Khosla, Michael Bernstein, Alexander C. Berg, and Li Fei-Fei. 2015. ImageNet Large Scale Visual Recognition Challenge. *International Journal of Computer Vision (IJCV)* 115, 3 (2015), 211–252. <https://doi.org/10.1007/s11263-015-0816-y>
- [51] Raimondo Schettini, Gianluigi Ciocca, Silvia Zuffi, Istituto Tecnologie, Infomatiche Multimediali, and Consilio Ricerche. 2001. A Survey Of Methods For Colour Image Indexing And Retrieval In Image Databases. (02 2001).
- [52] Thibault Sellam, Kevin Lin, Ian Huang, Michelle Yang, Carl Vondrick, and Eugene Wu. 2019. Deepbase: Deep inspection of neural networks. In *Proceedings of the 2019 International Conference on Management of Data*. 1117–1134.
- [53] Ramprasaath R. Selvaraju, Michael Cogswell, Abhishek Das, Ramakrishna Vedantam, Devi Parikh, and Dhruv Batra. 2017. Grad-CAM: Visual Explanations from Deep Networks via Gradient-Based Localization. In *2017 IEEE International Conference on Computer Vision (ICCV)*. 618–626. <https://doi.org/10.1109/ICCV.2017.74>
- [54] Sahil Singla, Eric Wallace, Shi Feng, and Soheil Feizi. 2019. Understanding Impacts of High-Order Loss Approximations and Features in Deep Learning Interpretation. [arXiv:1902.00407 \[cs.LG\]](https://arxiv.org/abs/1902.00407)
- [55] Daniel Smilkov, Nikhil Thorat, Been Kim, Fernanda Viégas, and Martin Wattenberg. 2017. Smoothgrad: removing noise by adding noise. *arXiv preprint arXiv:1706.03825* (2017).
- [56] Mukund Sundararajan, Ankur Taly, and Qiqi Yan. 2017. Axiomatic attribution for deep networks. In *International conference on machine learning*. PMLR, 3319–3328.
- [57] Manasi Vartak, Joana M F. da Trindade, Samuel Madden, and Matei Zaharia. 2018. Mistique: A system to store and query model intermediates for model diagnosis. In *Proceedings of the 2018 International Conference on Management of Data*. 1285–1300.
- [58] Manasi Vartak, Harihar Subramanyam, Wei-En Lee, Srinidhi Viswanathan, Saadiyah Husnoo, Samuel Madden, and Matei Zaharia. 2016. ModelDB: a system for machine learning model management. In *Proceedings of the Workshop on Human-In-the-Loop Data Analytics*. 1–3.
- [59] Shen Wang and Yuxin Gong. 2022. Adversarial example detection based on saliency map features. *Applied Intelligence* (2022), 1–14.
- [60] Julia K Winkler, Christine Fink, Ferdinand Toberer, Alexander Enk, Teresa Deinlein, Rainer Hofmann-Wellenhof, Luc Thomas, Aimilios Lallas, Andreas Blum, Wilhelm Stolz, et al. 2019. Association between surgical skin markings in dermoscopic images and diagnostic performance of a deep learning convolutional neural network for melanoma recognition. *JAMA dermatology* 155, 10 (2019), 1135–1141.
- [61] Weiyuan Wu, Lampros Flokas, Eugene Wu, and Jiannan Wang. 2020. Complaint-driven training data debugging for query 2.0. In *Proceedings of the 2020 ACM SIGMOD International Conference on Management of Data*. 1317–1334.
- [62] Doris Xin, Litian Ma, Jialin Liu, Stephen Macke, Shuchen Song, and Aditya Parameswaran. 2018. Accelerating human-in-the-loop machine learning: Challenges and opportunities. In *Proceedings of the second workshop on data management for end-to-end machine learning*. 1–4.
- [63] Dengpan Ye, Chuanxi Chen, Changrui Liu, Hao Wang, and Shunzhi Jiang. 2020. Detection Defense Against Adversarial Attacks with Saliency Map. [arXiv:2009.02738 \[cs.LG\]](https://arxiv.org/abs/2009.02738)
- [64] Chiliang Zhang, Zhimou Yang, and Zuochang Ye. 2018. Detecting Adversarial Perturbations with Saliency. In *Proceedings of the 6th International Conference on Information Technology: IoT and Smart City*. 25–30.
- [65] B. Zhou, A. Khosla, Lapedriza, A., A. Oliva, and A. Torralba. 2016. Learning Deep Features for Discriminative Localization. *CVPR* (2016).